RSC Advances

PAPER

View Article Online
View Journal | View Issue

Cite this: *RSC Adv.*, 2026, **16**, 5904

Plastic crystalline $[(C_4H_9)_4N]FeCl_4$: reversible order–disorder phase transitions and potential for thermal energy storage

Khawla Ben Brahim, *[a] Imen Ibrahmi,[a] Imed Kammoun, [a] Noweir Ahmad Alghamdi,[b] Jean-François Bardeau,[cd] Gwenaël Corbel [c] and Abderrazek Oueslati [a]

Alkylammonium halogenoferrates have attracted considerable attention due to their structural versatility and functional potential. Here, we report the growth of $[(C_4H_9)_4N]FeCl_4$ single crystals *via* slow evaporation under controlled conditions. X-ray powder diffraction (XRPD) confirmed the formation of a pure orthorhombic phase. Differential scanning calorimetry (DSC) revealed two reversible phase transitions between room temperature and 440 K, with a plastic crystalline state stabilized above 400 K. Temperature-controlled XRPD indicated a symmetry increase consistent with a phase transition, while Raman spectroscopy up to 423 K evidenced the reorientation of the tetrabutylammonium cation and displacement of the $[FeCl_4]^-$ anion as the driving mechanisms. The large enthalpy changes and reversible order–disorder dynamics highlight the potential of $[(C_4H_9)_4N]FeCl_4$ for thermal energy storage applications. Electrical characterization, performed through complex impedance measurements in the temperature range 303–393 K and frequency range 200–1 × 10^7 rad s^{-1}, confirmed the presence of two-phase transitions. The frequency-dependent AC conductivity follows Jonscher's universal power law and is governed by two hopping mechanisms: correlated barrier hopping (CBH) and non-overlapping small polaron tunneling (NSPT). Dielectric measurements further revealed relaxation processes consistent with the dynamic behavior of the cation–anion sublattice. These findings establish this hybrid halogenoferrate as a model system for probing phase-transition mechanisms in plastic crystalline materials and for designing next-generation thermal energy storage devices.

Received 20th December 2025
Accepted 16th January 2026

DOI: 10.1039/d5ra09848c

rsc.li/rsc-advances

1 Introduction

In recent years, hybrid halometallate systems have emerged as a promising class of organic–inorganic materials due to their adaptable structural characteristics, tunable physical and chemical properties, and potential applications in functional devices, electronics, and energy. Photovoltaics,[1,2] lithium batteries,[3] photomechanical actuators,[4] and low-melting ionic liquids[5] are among the applications enabled by their combination of coordination metal halide anions and organic cations. Of particular interest, these hybrids are increasingly investigated as high-conductivity solid-state electrolytes for batteries, fuel cells, and solar cells,[6] offering significant advantages over polymer electrolytes, which often suffer from low conductivity.[7]

Beyond ionic conduction, hybrid organic–inorganic systems have also attracted attention as phase-change materials (PCMs). Their reversible solid–solid transitions, often coupled with dielectric, magnetic, optical, or caloric responses, make them highly attractive for multifunctional devices including photonics, optoelectronics, sensors, memory units, and transducers.[8–10] These transitions typically involve reorientations of cationic and anionic subunits, in some cases, the globular and weakly bound nature of the constituents allows the formation of "plastic crystals." where molecules retain translational order while acquiring rotational freedom, resulting in unusual functional responses.[11,12] The relatively high latent heat associated with solid–plastic transitions further enhances their potential for thermal energy storage (TES) applications.[13–15]

Although hybrid plastic crystals remain rare, they have recently emerged as multifunctional candidates capable of combining TES with other physical properties.[16] For example, $[(C_nH_{2n+1})_4N]FeCl_4$ (n = 1, 2) compounds have been shown to exhibit coupled magnetic, optical, and dielectric switching, in addition to storing thermal energy.[15,17] Their TES potential is

[a]*Laboratory of Spectroscopic Characterization and Optical Materials, Faculty of Sciences, University of Sfax, B.P. 1171, 3000 Sfax, Tunisia. E-mail: benbrahimkhawla75@gmail.com*

[b]*Departement of Physics, Faculty of Science, Al-Baha University, Alaqiq, 65779, Saudi Arabia*

[c]*Institut des Molécules et Matériaux Du Mans (IMMM)– UMR-6283 CNRS, Le Mans Université, Avenue Olivier Messiaen, F-72085 Le Mans Cedex 9, France*

[d]*Université D'Orléans, CNRS, ICMN, UMR 7374, Orléans, France*

highlighted by the high latent heats accompanying temperatures their plastic transitions, which occur at approximately 386 K and 413 K, respectively. Crucially, these materials can be easily and affordably processed into thin films, which is essential for real-world uses.

In this context, we report the synthesis and characterization of the hybrid compound $[(C_4H_9)_4N]FeCl_4$. By extending the alkyl chain length, this compound exhibits plastic-crystal behavior with a pronounced enthalpy (~10 kJ kg^{-1}) and a transition temperature window between 380 and 404 K, meeting the requirements for commercial solar TES applications. The crystal structure of $[(C_4H_9)_4N]FeCl_4$ consists of tetrabutylammonium $[(C_4H_9)_4N]^+$ cations and tetrahedral $FeCl_4^-$ anions (Fig. 1).

All cations and anions lie on twofold axes of the orthorhombic space group *Pnna* (*n*°52). The phase transitions were identified by temperature-dependent X-ray diffraction and Raman spectroscopy, and are accompanied by reversible changes in dielectric and electrical conductivity. These results establish $[(C_4H_9)_4N]FeCl_4$ as a new multifunctional hybrid plastic crystal, bridging structural tunability with energy storage functionality.

2 Experimental

2.1 Synthetic procedures

Single crystals of $[(C_4H_9)_4N]FeCl_4$ were obtained by slow evaporation at room temperature. Almost saturated aqueous solutions of stoichiometric amounts of $FeCl_3$ (0.1 g, 6.16 × 10^{-4} mol) and $[(C_4H_9)_4N]Cl$ (0.171 g, 6,16 × 10^{-4} moles) were prepared.

The subsequent chemical reaction sequence is the following:

The mixture was stirred for several minutes to ensure homogeneity and then left to evaporate slowly at a constant temperature of 30 °C. After 2–4 days, green–yellow crystals suitable for single-crystal X-ray diffraction appeared and gradually increased in size.

2.2 Characterizations

A portion of the millimetre-sized crystals of $[(C_4H_9)_4N]FeCl_4$ has been crushed into micrometric powder in order to verify sample purity by X-ray powder diffraction (XRPD). The pattern was recorded at room temperature on a PANalytical θ/θ Bragg–Brentano Empyrean diffractometer (CuKα_{1+2} radiations) equipped with the PIXcel^{1D} detector. The data were collected in the [5°–100°] scattering angle range, with a 0.0131° step size, for a total acquisition time of 10 h.

Previous DSC investigations on $[(C_4H_9)_4N]FeCl_4$ reported two endothermic transitions upon heating at 379 and 409 K (106 and 136 °C), and corresponding exothermic events upon cooling near 341 and 390 K (68 and 117 °C).[18] These results suggested reversible phase transitions, but their origin remained unclear.

In the present study, DSC measurements were performed using a PerkinElmer DSC-7 instrument. Approximately 8 mg of finely ground sample was sealed in a 40 μL aluminum crucible with a pierced cap. The measurements were carried out over the 293–443 K range, at a heating and cooling rate of 5 K min^{-1} under a constant flow of dry nitrogen gas. Reproducibility was confirmed by performing two heating–cooling cycles.

Variable-temperature XRPD measurements were performed on the same diffractometer equipped with an Anton Paar XRK 900 reactor chamber, enabling temperature control between 298 and 378 K. The sample was deposited on a glass-ceramic Macor® sieve (pore size 0.2 mm) mounted in an open sample holder, allowing air flow through the specimen. Data were collected under an air flow of 40 mL min^{-1} with a heating rate of 5 K min^{-1} (20 min stabilization at each temperature) and a cooling rate of 60 K min^{-1}. For each selected temperature, diffraction patterns were recorded over the 2θ range 7–48° with a step size of 0.0131° and a total acquisition time of 95 min.

Raman spectra of $[(C_4H_9)_4N]FeCl_4$ were recorded using a T-64000 spectrometer (Jobin-Yvon, Horiba Group, Kyoto, Japan) with excitation at 647.1 nm provided by an argon–krypton ion laser (Innova, Coherent, France). The laser was focused onto the sample through a BX41 Olympus microscope equipped with a MSPlan 50× objective (N.A. 0.55). The laser power was kept below 2 mW to prevent sample damage. Spectra were collected twice at each point with an integration time of 60 s. Scattered light was dispersed by a single monochromator (600 grooves per mm) and detected with a nitrogen-cooled, front-illuminated CCD detector. The spectral range was 70–3100 cm^{-1}, and the temperature range was 298–423 K. Raman spectra were analyzed using LabSpec V5.25 (Jobin-Yvon, Horiba Group). Peak positions and full width at half maximum (FWHM) were determined by fitting Lorentzian line shapes.

To examine the dielectric characteristics of $[(C_4H_9)_4N]FeCl_4$, a pellet was made by compressing the powder into an 8 mm diameter and 1.1 mm thick circular disc while applying a pressure of 5 tons per centimeter. A Solartron impedance analyzer was used to conduct electrical measurements over a frequency range of 200 to 1 × 10^7 rad s^{-1} with an applied AC voltage of 50 mV.

At temperatures higher than 398 K, the pellet showed greater pliability during the measurements, indicating plastic behavior in the organic–inorganic crystals. As a result, only up to 393 K could dielectric characterization be done with confidence.

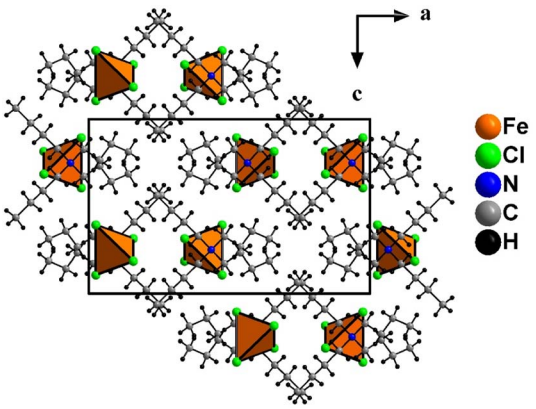

Fig. 1 Projection of the crystal structure of $[(C_4H_9)_4N]FeCl_4$ in the (ac) plane.

$$[(C_4H_9)_4N]Cl + FeCl_3 \xrightarrow{H_2O} [(C_4H_9)_4N]\,FeCl_4$$

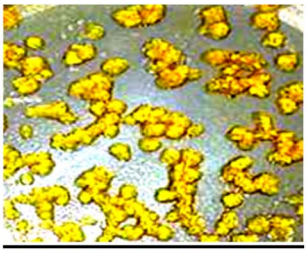

3 Results and discussion

3.1 X-ray powder diffraction analysis

Few randomly selected crystals of the preparation were ground and then analysed by X-ray powder diffraction (XRPD). The X-ray powder diffraction (XRPD) pattern of $[(C_4H_9)_4N]FeCl_4$ was recorded at room temperature, as shown in Fig. 2. All peaks observed in the XRPD pattern can be indexed with the unit cell parameters and the orthorhombic *Pnna* (*n*°52) space group reported by Hay *et al.*[19] The cell parameters determined from the refinement of the XRPD pattern by the Le Bail method[20] of the Fullprof program[21] are $a = 18.4460(7)$ Å, $b = 11.5316(5)$ Å and $c = 11.4121(4)$ Å. These values are close to those obtained by Hay *et al.*[19] from the single-crystal XRD data of $[(C_4H_9)_4N]FeCl_4$. Consequently, slow evaporation of a solution containing $FeCl_3$ and $[(C_4H_9)_4N]Cl$ salts leads only to the formation of the compound $[(C_4H_9)_4N]FeCl_4$.

3.2 Thermal analysis

The DSC thermogram of $[(C_4H_9)_4N]FeCl_4$ (Fig. 3) reveals two reversible endothermic transitions upon heating at 378 and 400 K, with corresponding exothermic events during cooling at 355 and 378 K, indicating thermal hysteresis of 23 and 22 K, respectively (Table 1). These transition temperatures are comparable to those reported for other hybrid molecular crystals exhibiting reversible order–disorder phase transitions.[22,23] In particular, $[(C_2H_5)_4N]FeCl_4$ shows phase transitions around 318 and 396 K, while $[(CH_3)_4N]FeCl_4$ exhibits multiple transitions at approximately 312, 347, and 386 K.[17,25]

With M ($[(C_4H_9)_4N]\,FeCl_4$) = 440.12074 g mol^{-1}.

The associated entropy changes, ΔS, yield configurational numbers of states, N, of 5.088 and 8.465, reflecting a substantial increase in accessible configurations in the high-temperature phase, characteristic of plastic crystals.

The first transition at $T_1 = 378$ K is attributed to rotational activation of the $FeCl_4^-$ anion, consistent with previous observations in $[(CH_3)_4N]FeCl_4$ (ref. 25) and $[(C_2H_5)_4N]FeCl_4$.[17] The high-temperature phase is locally disordered, resulting from rotational freedom of both the $[FeCl_4]^-$ anions and the $[(C_4H_9)_4N]^+$ cations. The large entropy changes confirm that both anomalies correspond to order–disorder transitions into a plastic state.[24,26] Minor variations in peak shapes between the first and second heating cycles indicate that partial dehydration does not alter the number of transitions but helps stabilize the material.

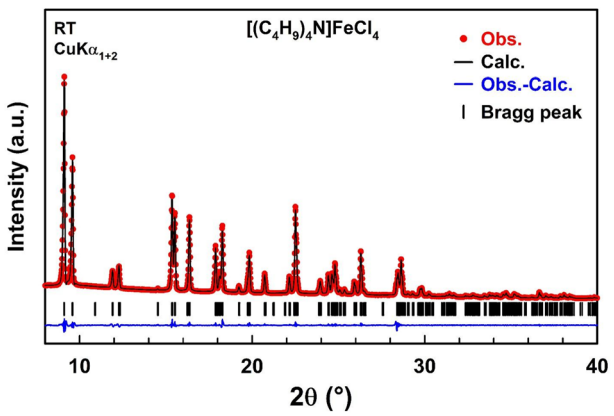

Fig. 2 Comparison of the observed diffraction pattern of $[(C_4H_9)_4N]FeCl_4$ (red dots) with the pattern calculated by the Le Bail method (black line). The blue curve corresponds to the difference between observed and calculated patterns. Vertical markers give Bragg peak positions (space group *Pnna* (*n*°52)).

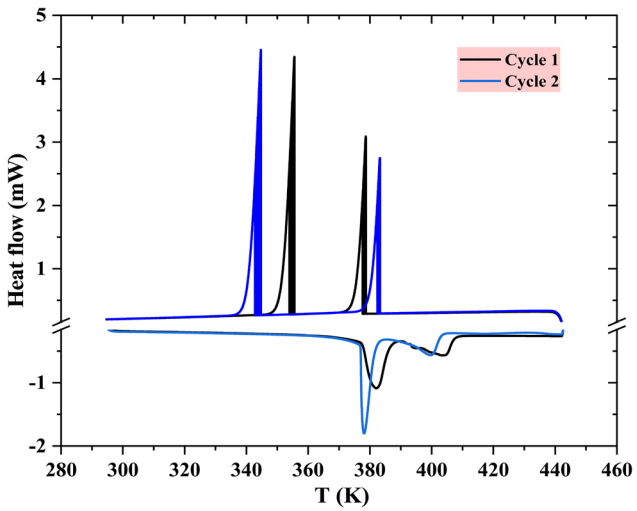

Fig. 3 DSC thermogram collected under N_2 on crushed crystals of $[(C_4H_9)_4N]FeCl_4$.

Table 1 Heat exchanges and nature of phase transitions in $[(C_4H_9)_4N]FeCl_4$

[293–443 K] (cycle 1)							
Heating					Cooling		
T (K)	ΔH (kJ mol^{-1})	ΔS (J mol^{-1} K^{-1})	N	Nature of transition	T (K)	ΔH (kJ mol^{-1})	ΔS (J mol^{-1} K^{-1})
382	4.209	11.018	3.599	Order–disorder	344	5.157	14.991
404	11.284	27.93	9.131	Order–disorder	383	9.122	23.817
[293–443 K] (cycle 2)							
Heating					Cooling		
T (K)	ΔH (kJ mol^{-1})	ΔS (J mol^{-1} K^{-1})	N	Nature of transition	T (K)	ΔH (kJ mol^{-1})	ΔS (J mo^{-1} K^{-1})
378	5.883	15.564	5.088	Order–disorder	355	5.383	15.163
400	10.356	25.89	8.465	Order–disorder	378	10.136	26.815

3.3 Temperature-controlled X-ray powder diffraction

Temperature-controlled X-ray powder diffraction (XRPD) patterns of $[(C_4H_9)_4N]FeCl_4$ were collected between 298 and 383 K (Fig. 4) to investigate structural changes associated with the transition at T_1 = 378 K measured by DSC. The XRPD data collection were limited to 383 K to prevent reactions between the compound and the glass-ceramic sample holder. A total of 27 patterns were recorded at 2–5 K intervals.

Fig. 4 shows the thermal evolution of the XRPD diagrams of $[(C_4H_9)_4N]FeCl_4$ in the range 298–383 K. The XRPD patterns collected above 376 K differ from those collected below 343 K. These patterns above 376 K can only be attributed to a high temperature crystallographic form of $[(C_4H_9)_4N]FeCl_4$, as no decomposition occurs in this temperature range according to ref. 18. It confirms the existence of structural phase transition, as detected at 378 K by DSC.

More specifically, upon heating above 376 K, several characteristic reflections located at $2\theta \approx 16.25°$, 20.62°, 24.71°, 28.36°, and 29.62° progressively weaken and disappear. The extinction of these peaks, together with the overall reduction in the number of diffraction reflections and partial peak merging, provides direct evidence of a symmetry increase, consistent with a transition from a low-symmetry phase to a higher-symmetry crystallographic form.

In the temperature range between 343 and 376 K, the XRPD patterns result from the superposition of the patterns of the two forms (*i.e.* low and high temperature) of $[(C_4H_9)_4N]FeCl_4$. This coexistence is due to a progressive and slow conversion of the low-temperature form into the high-temperature form. It should be noted that the endothermic peak at 378 K is quite large when the $[(C_4H_9)_4N]FeCl_4$ powder is heated at 10 K min^{-1} during the first cycle of DSC measurements and much narrower during the second cycle. A much slower conversion is likely in the temperature-controlled powder X-ray diffraction experiment, as the patterns were recorded for 95 minutes at several temperatures with a lower heating rate (5 K min^{-1}) than that used in the DSC experiment. Such smooth transition could be due to progressive displacements/reorientations of the $[(C_4H_9)_4N]^+$ cations and tetrahedral $FeCl_4^-$ anions in the crystal structure of $[(C_4H_9)_4N]FeCl_4$. The Raman spectroscopy will later give evidence for such displacements/reorientations. It is very

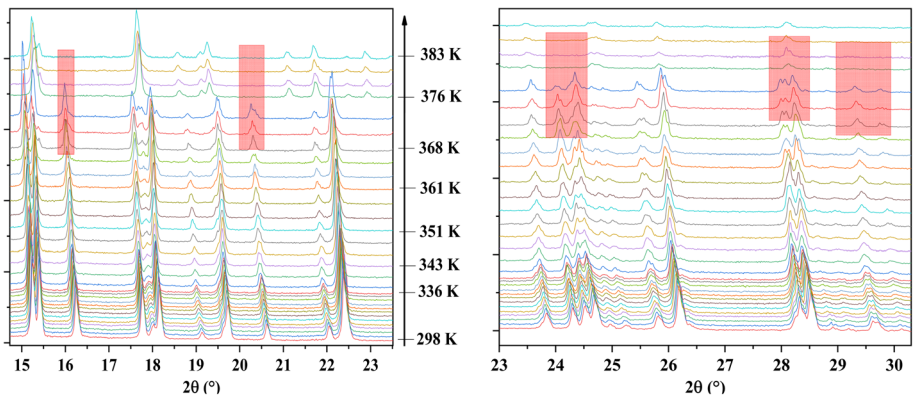

Fig. 4 XRPD patterns recorded during heating of the $[(C_4H_9)_4N]FeCl_4$ powder in air from 298 to 383 K.

difficult to determine the crystal structure of an inorganic–organic compound from the Rietveld refinement of XRPD data. This is why we did not attempt to determine the crystal structure of the high-temperature form of $[(C_4H_9)_4N]FeCl_4$, existing above 376 K, from the XRPD data.

Only refinements of the XRPD patterns collected below 343 K were carried out by the Le Bail method. Successively, the orthorhombic cell parameters determined from the refinement of a lower temperature XRPD pattern was used as starting values for the refinement of the next higher temperature pattern. All XRPD patterns can be satisfactorily fitted in this way, confirming that the low temperature crystal structure of $[(C_4H_9)_4N]FeCl_4$ is preserved in the temperature range 298–343 K. The thermal evolutions of the cell parameters of the low-temperature form are displayed in Fig. 5. The three orthorhombic cell parameters linearly increase with temperature in the range 298–343 K. From these linear evolutions, thermal expansion coefficients (TEC) along the different crystallographic axes are calculated: $TEC_a = 35.03 \times 10^{-2}\ K^{-1}$, $TEC_b = 12.75 \times 10^{-2}\ K^{-1}$ and $TEC_c = 11.67 \times 10^{-2}\ K^{-1}$. Thermal expansion in the [100] direction is more than two times greater than in the basal plane (bc).

3.4 Raman spectroscopy as a function of temperature

The temperature evolution of the Raman spectra of $[(C_4H_9)_4N]FeCl_4$ was investigated from 298 to 423 K (Fig. 6–8). For clarity, the spectra are shown in three wavenumber ranges, omitting regions without bands. At room temperature, the bands of the $[FeCl_4]^-$ anion (70–400 cm^{-1}) and the $[(C_4H_9)_4N]^+$ cation (>400 cm^{-1}) were assigned based on previous literature[27–32] (Table 2).

Between 300 and 370 K, the crystal remains stable. Near $T_1 =$ 378 K, the symmetric deformation mode $\delta_s(FeCl_4^-)$ shifts ~2 cm^{-1} to higher frequencies and narrows by 3 cm^{-1}, while $\delta_{as}(FeCl_4^-)$ shifts by 1 cm^{-1} and broadens by 5 cm^{-1}. The symmetric stretching mode $\nu_s(FeCl_4^-)$ at 266 cm^{-1} shifts +1 cm^{-1} at T_1 and −2 cm^{-1} at $T_2 = 400$ K. The cationic bands are also affected: δ(C–C–C) at 883 cm^{-1} shifts to lower frequency with discontinuities at T_1 and T_2, with the width increasing by 9 cm^{-1} after T_2; ν_s(N–C) shows a 2 cm^{-1} jump at T_1 and narrows by 6 cm^{-1} near T_2. Several C–C stretching modes disappear above T_1, while δ(C–C–C) + δ(C–N–C) and $\delta(CH_3)$ + $\delta(CH_2)$ broaden by 2–6 cm^{-1} before T_2.

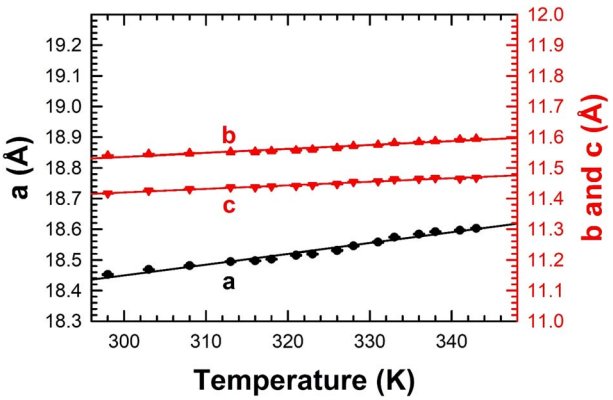

Fig. 5 Thermal evolutions of the orthorhombic cell parameters *a*, *b* and *c* of the low temperature form of the $[(C_4H_9)_4N]FeCl_4$ compound determined from the refinement by the Le Bail method of the XRPD patterns collected in the temperature range 298–343 K.

These changes clearly demonstrate two reversible phase transitions at $T_1 = 378$ K and $T_2 = 400$ K, consistent with DSC measurements. The transitions are associated with rotational and reorientational motions of both the $[(C_4H_9)_4N]^+$ cations and $[FeCl_4]^-$ anions. In particular, T_1 corresponds to thermal activation of $FeCl_4^-$ rotations, as observed in $[(CH_3)_4N]FeCl_4$ and $[(C_2H_5)_4N]FeCl_4$.[17,25] The increased peak widths above 400 K and the tendency towards a highly symmetric cubic phase indicate the formation of a plastic crystal state, in agreement with the large entropy changes observed in DSC.

3.5 Electric properties

3.5.1 AC electrical conductivity. The AC conductivity (σ_{ac}) was evaluated from the complex impedance data using the well-established relation. Fig. 9 illustrates the frequency dependence of σ_{ac} at different temperatures. The conductivity spectra clearly exhibit two regions: a frequency-independent plateau at low frequencies, followed by a strong dispersive increase at higher frequencies. The low-frequency plateau corresponds to the dc conductivity regime, where the applied field drives charge carriers over long distances, enabling long-range translational motion.[33] At elevated frequencies, however, the conductivity rises due to localized hopping or reorientation of charge carriers over shorter distances, producing a dispersive behavior.[34–36]

This frequency dependence is well described by Jonscher's universal power law:[37]

$$\sigma_{ac}(\omega) = \sigma_{dc} + A\omega^s \quad (1)$$

where σ_{dc} represents the frequency-independent conductivity at low frequencies, A is a temperature-dependent constant, and s ($0 < s < 1$) is the frequency exponent that provides information on the conduction mechanism. The increase of conductivity with frequency can thus be attributed to the enhancement of the hopping frequency of charge carriers, which accelerates charge transport and strengthens the conduction process. Furthermore, the overall temperature dependence of σ_{ac} indicates a thermally activated transport mechanism, consistent with the idea that increasing temperature supplies additional energy to the carriers, enabling them to overcome potential barriers.

The temperature dependence of DC conductivity, plotted as $\ln(\sigma_{dc}T)$ *versus* $1000/T$ (Fig. 10), reveals a clear increase in conductivity with rising temperature, indicating thermally activated charge transport consistent with Arrhenius behavior:

$$\sigma_{dc} \times T = \sigma_0 \exp\left(-\frac{E_a}{k_B T}\right) \quad (2)$$

where E_a is the activation energy, k is the Boltzmann constant, and T is the absolute temperature.

Three distinct conduction regions, labeled I, II, and III, are observed, separated by slope changes at $T_1 = 343$ K and $T_2 = 378$

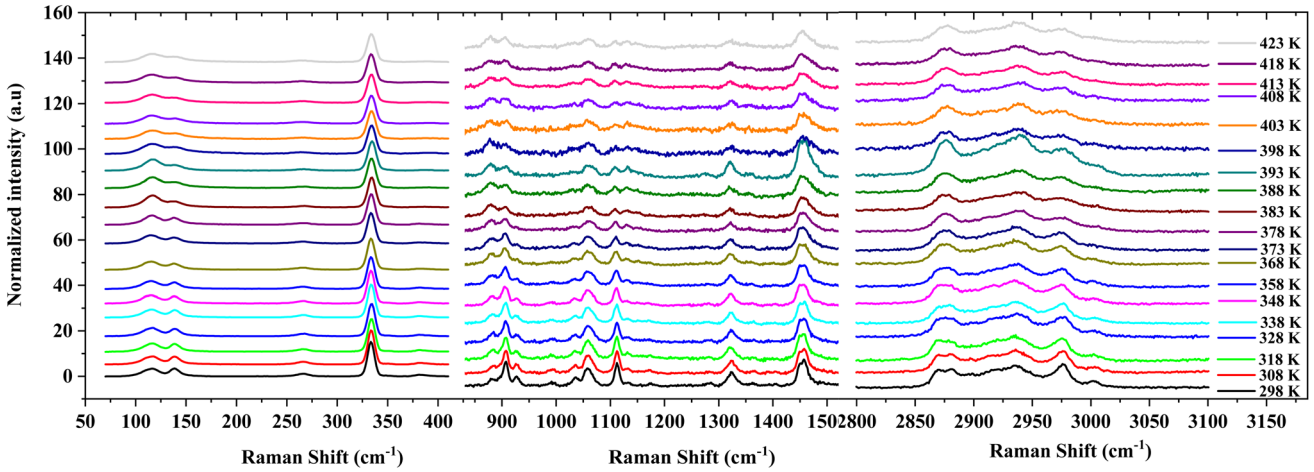

Fig. 6 Raman spectra of $[(C_4H_9)_4N]FeCl_4$ compound between 298 and 423 K. Spectral regions without observable bands have been omitted.

K which may be corresponding to a conduction-related phase transition in the material. Linear fits in these regions yield the activation energies: $E_{a1} = 0.21$ eV, $E_{a2} = 0.58$ eV, and $E_{a3} = 1.71$ eV. The progressive increase in activation energy from region I to III indicates that proton transport requires overcoming increasingly significant energy barriers.[35]

3.5.2 Theory investigation of the conduction mechanism. The AC conductivity spectra were successfully analyzed using the Jonscher equation (eqn (1)), showing good agreement between the experimental data and the theoretical fits, and enabling the extraction of the frequency exponent s at different temperatures. The exponent s has a clear physical meaning: values of $s < 1$ correspond to a translational hopping mechanism involving long-range motion of charge carriers, whereas $s > 1$ indicates localized hopping characterized by short-range motion within the vicinity of the charge carriers. To identify the dominant conduction mechanism in $[(C_4H_9)_4N]FeCl_4$, several theoretical models proposed by Long *et al.* were considered to correlate the AC conduction process with the temperature dependence of s, including the Quantum Mechanical Tunneling (QMT), Overlapping Large Polaron Tunneling (OLPT), Non-overlapping Small Polaron Tunneling (NSPT), and Correlated Barrier Hopping (CBH) models.[36–38]

Fig. 11 depicts the temperature dependence of the exponent s, which exhibits a pronounced non-monotonic behavior, revealing the coexistence of two distinct conduction mechanisms across different temperature regions.

In regions I and III, the exponent s decreases with increasing temperature, indicating that the CBH model governs the charge transport in these phases. Within this framework, charge carriers hop between localized states by surmounting potential barriers, with the hopping probability being strongly temperature-dependent. In contrast, in region II, s increases with rising temperature, suggesting that the NSPT model is the

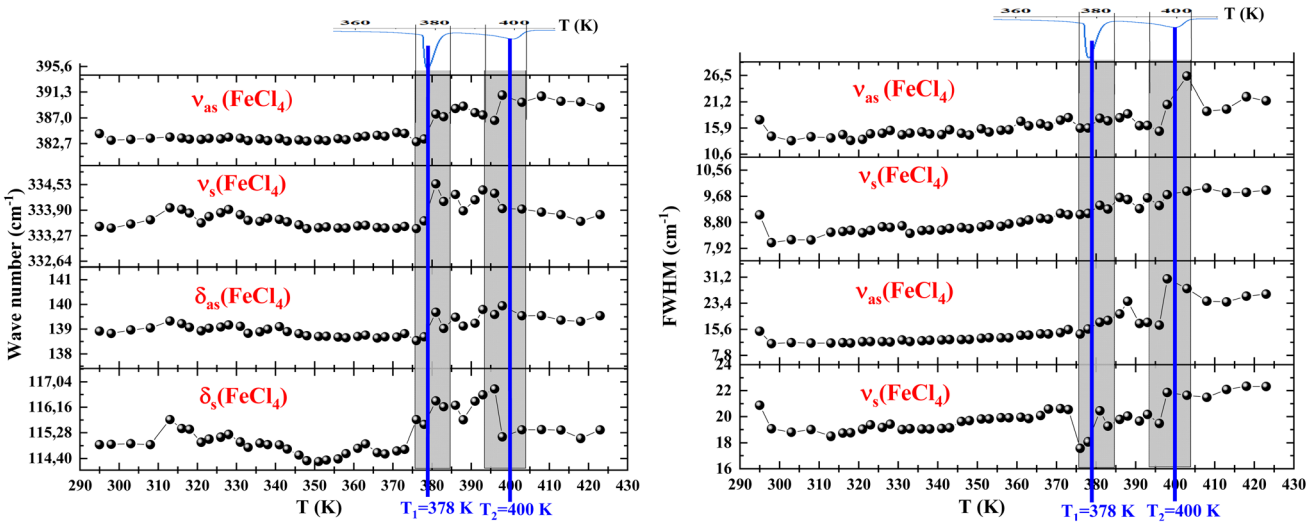

Fig. 7 Temperature dependence of the positions and full width at half maximum (FWHM) of the Raman vibrational bands of the inorganic component. (DSC transitions in blue vertical lines).

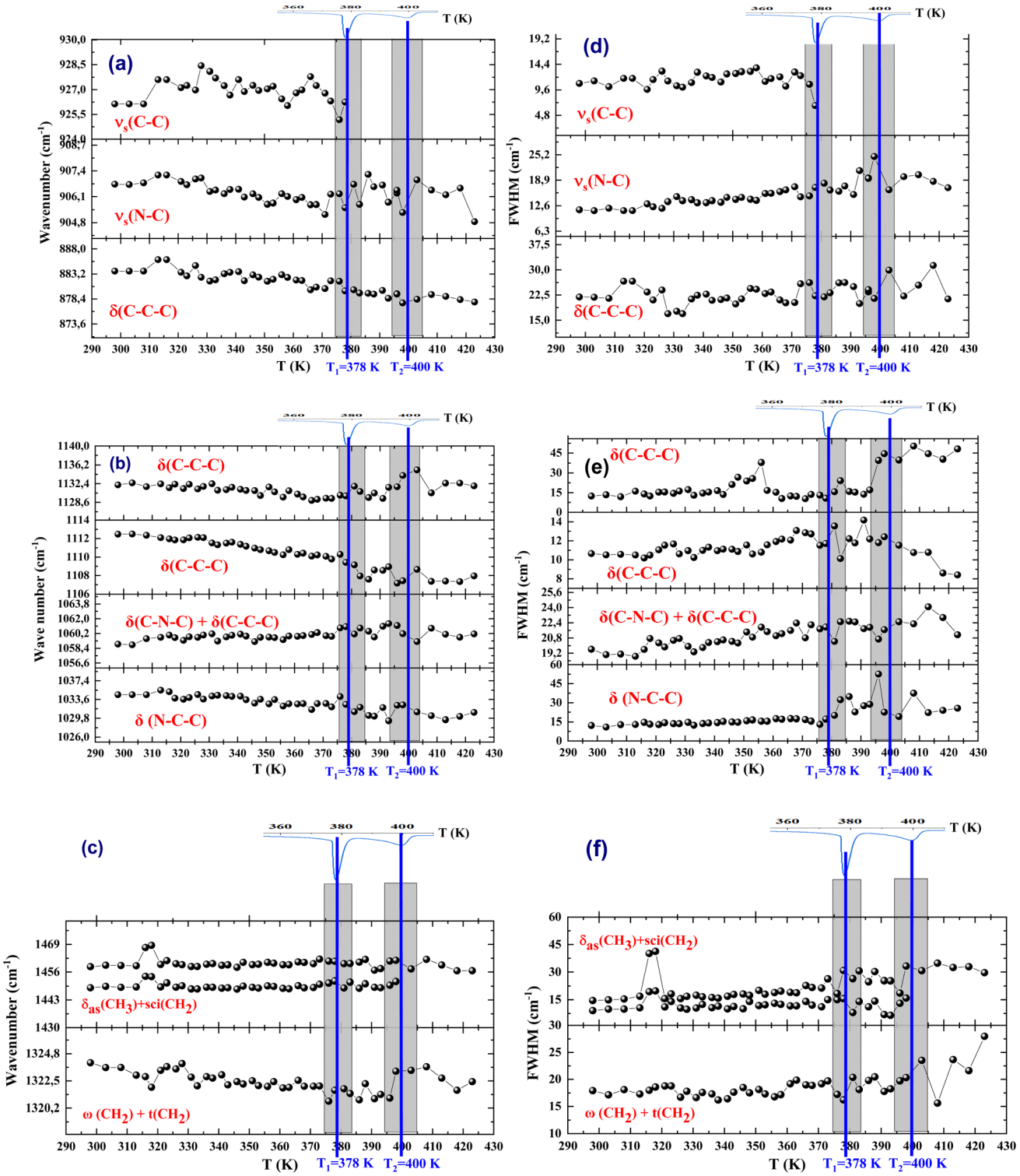

Fig. 8 (a–c) Temperature dependence of the positions and full width at half maximum (FWHM) (d–f) of the Raman vibrational bands of $[(C_4H_9)_4N]^+$. (DSC transitions in blue vertical lines).

most appropriate to describe the electrical conduction mechanism in this phase. This behavior is characteristic of thermally activated small-polaron transport, where polarons tunnel between localized sites without significant wave-function overlap, rendering the conduction process weakly dependent on the inter-site distance. Overall, these findings demonstrate that the AC conductivity of $[(C_4H_9)_4N]FeCl_4$ is governed by a temperature-dependent interplay between hopping and tunneling mechanisms, with CBH dominating at low and high temperatures (regions I and III) and NSPT prevailing at intermediate

Table 2 The observed bands at room temperature[a]

Wavenumber (cm^{-1})	Vibrational mode	Intensity
115	$\delta_s(FeCl_4)$	Mean
138	$\delta_{as}(FeCl_4)$	Mean
333	$\nu_s(FeCl_4)$	Forte
382	$\nu_{as}(FeCl_4)$	Weak
453		Weak
523		Weak
597		Weak
740	$\nu(NC_4)$	Weak
778	$\nu(NC_4)$	Weak
883	δ(C–N–C)+ δ(C–C–C)	Mean
904	ν_s(N–C)	Forte
926	ν_s(C–C)	Mean
992	δ(C–N–C) + ν(C–C)	Weak
1035	δ(C–C–C) + δ(C–N–C) + ν(C–C) + δ(N–C–C)	Mean
1057	δ(C–N–C) + δ(C–C–C)	Strong
1112	δ(C–C–C)	Strong
1131	δ(C–C–C)	Weak
1173	$t(CH_2)$	Weak
1284	$\omega(CH_2)$	Weak
1323	$\omega(CH_2)$ + $t(CH_2)$	Mean
1362	$\omega(CH_2)$	Weak
1405	$\delta_{as}(CH_3)$	Weak
1454	$\delta_{as}(CH_3)$ + sci(CH_2)	Strong
2870	$\nu_s(CH_2) - \nu_s(CH_3)$	Mean
2880	$\nu_s(CH_2) - \nu_s(CH_3)$	Mean
2918	$\nu_{as}(CH_2)$	Mean
2935	$\nu_{as}(CH_2)$	Mean
2976	$\nu_{as}(CH_3)$	Mean
3000	$\nu_{as}(CH_2) + \nu_{as}(CH_3)$	Weak

[a] ν_s: symmetrical stretch; ν_{as}: asymmetrical stretch; δ_s: symmetric deformation; δ_{as}: asymmetric deformation; t: twisting; ρ: rotation; ω: wagging.

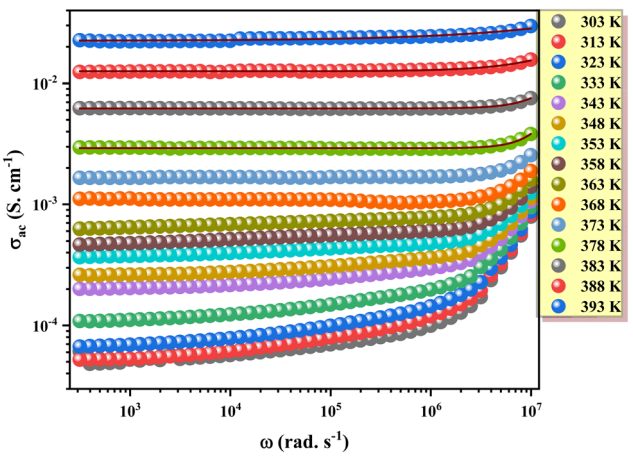

Fig. 9 The frequency-dependent conductivity data, which are fitted to Jonscher's universal power law.

temperatures (region II). The observed change in the slope of $s(T)$ around 343 K is therefore directly associated with a transition in the conduction mechanism, providing deeper insight into the microscopic charge transport processes within the material.

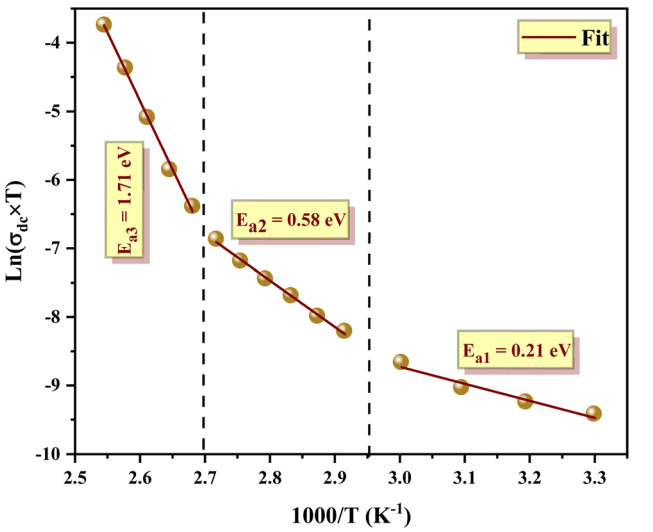

Fig. 10 Variation of the ln($\sigma_{dc}T$) *versus* 1000/T of the $[(C_4H_9)_4N]FeCl_4$ compound.

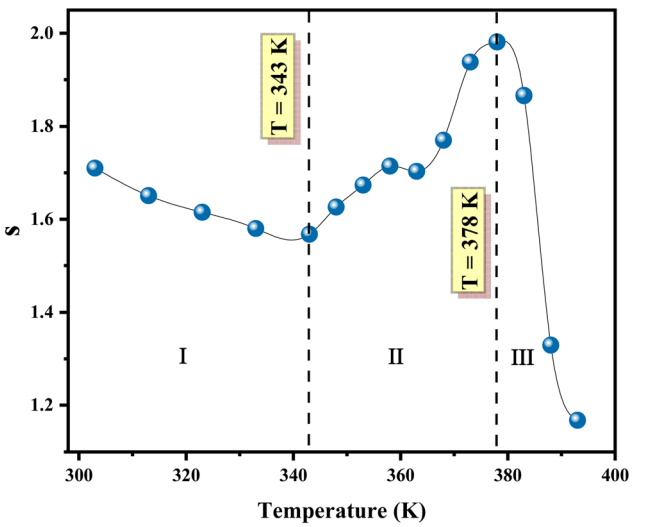

Fig. 11 Temperature dependence of the exponent s.

3.5.3 Dielectric properties. The dielectric characteristics of materials are intrinsically linked to their molecular characteristics and play a central role in systems where electron mobility can occur. When subjected to an external electric field, this mobility induces polarization within the material. The delayed response of the dipoles, often referred to as charge moment inertia, leads to polarization relaxation phenomena.[39]

Dielectric relaxation is therefore a powerful tool for probing the underlying mechanisms of electrical conduction, identifying the origin of dielectric losses, and providing valuable insight into structural transformations such as phase transitions, which are also evidenced by the DSC curve.

The complex dielectric function is expressed as:

$$\varepsilon^* = \varepsilon' - i\varepsilon''$$

where ε' is the real part of the dielectric constant (related to the material's ability to store electric energy) and ε'' is the imaginary part of the dielectric constant (related to the material's ability to dissipate electric energy as heat).

The temperature evolution of the real ε' and imaginary ε'' components of the dielectric permittivity for the investigated compound is presented in Fig. 12(a) and (b). At temperatures below 340 K, both ε' and ε'' remain nearly constant. This behavior can be attributed to the restricted reorientational motion of the organic $[(C_4H_9)N]^+$ cations and the inorganic $[FeCl_4]^-$ anions, which are unable to align with the applied electric field and thus contribute only weakly to the overall polarization.[40,41]

A change in the conduction mechanism is responsible for a minor anomaly in ε' that was discovered at around 343 K. On the other hand, the sharp rise in both ε' and ε'' around 378 K supports the crystalline dynamics observed in both Raman and XRD studies as well as with the phase transition detected by DSC. The cations' reorientational dynamics are thermally activated as the temperature rises over 378 K. The cations can more readily reorient under the external field when sufficiently excited thermally, which increases their contribution to polarization and raises the dielectric response noticeably. Lastly, the compound's increased electrical conductivity, which is controlled by charge carrier motion, is directly linked to the decrease in ε' and ε'' with increasing frequency.

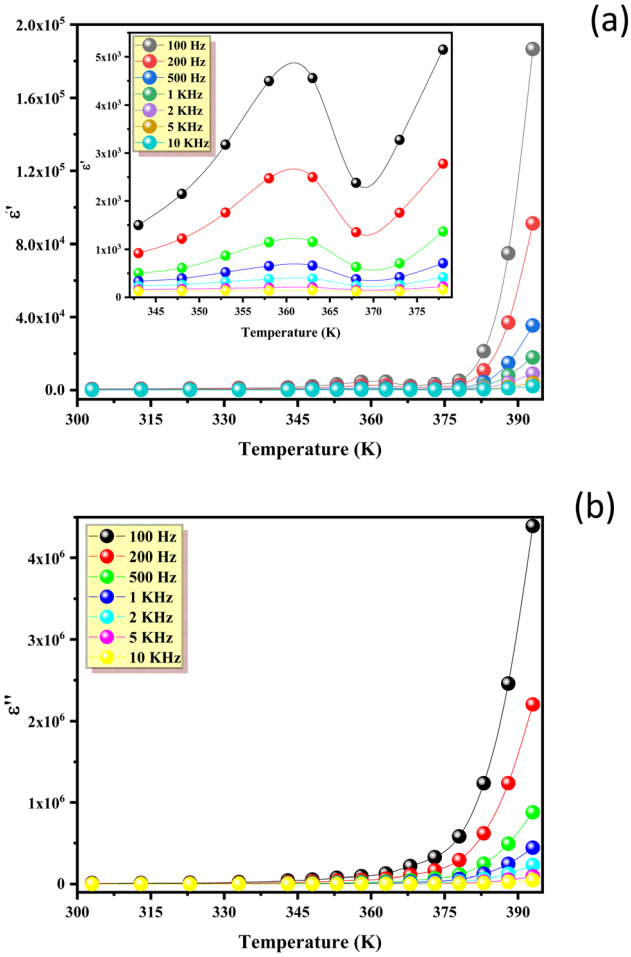

Fig. 12 Temperature dependence of (a) the dielectric constant ε' and (b) the dielectric loss ε'' at different frequencies for $[(C_4H_9)_4N]FeCl_4$.

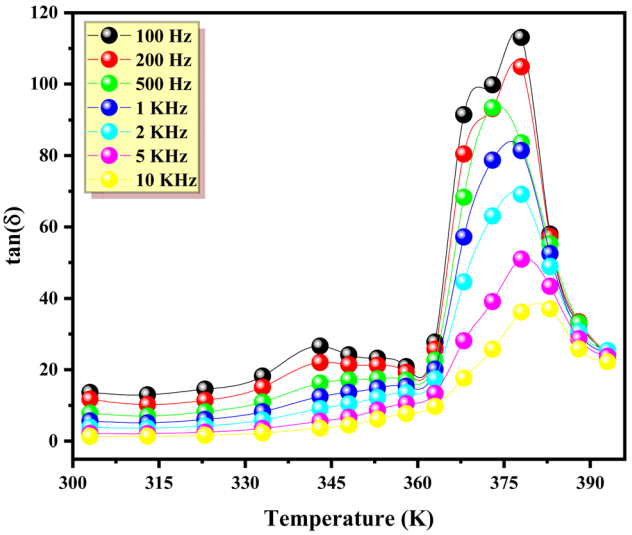

Fig. 13 Temperature dependence of tan(δ) at different frequencies for $[(C_4H_9)_4N]FeCl_4$.

The dielectric losses were further analyzed through the dissipation factor (tan δ), defined as the ratio of the imaginary permittivity to the real permittivity:[42]

$$\tan(\delta) = \frac{\varepsilon''}{\varepsilon'}$$

Fig. 13 illustrates the variation of tan(δ) with temperature at different frequencies. The dielectric loss exhibits a similar temperature-dependent trend as ε', confirming the strong correlation between polarization processes and charge transport.

Moreover, the increase in tan(δ) values at higher temperatures indicates a growing contribution from conductivity, reinforcing the mixed dielectric-conductive nature of the relaxation mechanism in this material.

4 Conclusion

Our work presents $[(C_4H_9)_4N]FeCl_4$ as a unique plastic crystal exhibiting intriguing functional properties, with potential for multi-energy storage applications, including both electrical and thermal energy storage. The compound undergoes two reversible, first-order phase transitions near 378 and 400 K, characterized by notable latent heats ($\Delta H = 15.564$ and 30.415 J mol^{-1} K^{-1}) and relatively large thermal hysteresis (23 and 22 K). Electrical and dielectric analyses indicate that charge transport follows a combination of correlated barrier hopping (CBH) and non-overlapping small polaron tunneling (NSPT) mechanisms, while dielectric relaxation reflects its dynamic behavior.

Comprehensive investigations combining DSC, temperature-dependent XRPD, Raman spectroscopy, and dielectric

measurements reveal that these phase transitions are driven by order–disorder dynamics, involving both the rotational flexibility of the tetrabutylammonium cation and the reorientational dynamics of the $[FeCl_4]^-$ anion. The strong coupling between the organic and inorganic sublattices is evident from the consistent behavior observed across structural, vibrational, and dielectric measurements.

These features, together with the large enthalpy changes and reversible plastic behavior, make $[(C_4H_9)_4N]FeCl_4$ a promising candidate for thermal energy storage, with an operating temperature window between 378 and 400 K. Beyond thermal applications, this compound provides valuable insights into dynamic disorder in hybrid plastic crystals and holds potential for advanced ionic conductors, sensors, and switchable capacitors. While additional studies are warranted to fully explore the plastic crystalline state, $[(C_4H_9)_4N]FeCl_4$ represents a versatile platform for future multifunctional applications.

Author contributions

Khawla BEN BRAHIM: investigation (synthesis, impedance spectroscopy, Raman and diffraction), writing- original draft and writing – review & editing. Imen IBRAHMI: formal analysis and data curation (diffraction). Imed KAMMOUN formal analysis, validation, writing review. Noweir Ahmad ALGHAMDI: formal analysis, validation, writing review. Jean-François BARDEAU: investigation, formal analysis and data curation (Raman spectroscopy), writing-original draft, writing – review & editing. Gwenaël CORBEL: investigation, formal analysis and data curation (thermal analyses and diffraction), writing-original draft, writing – review & editing. Abderrazek OUESLATI: writing–review & editing, visualization, validation, investigation, formal analysis.

Conflicts of interest

The authors declare that they have no known competing financial interests or personal relationships that could have appeared to influence the work reported in this paper.

Data availability

The authors confirm that the data used to support the findings of this study are included within the article and are available from the corresponding author upon reasonable request.

References

1 T. AlZoubi, B. Mourched, M. Al Gharram, G. Makhadmeh and O. Abu Noqta, Improving Photovoltaic Performance of Hybrid Organic-Inorganic MAGeI3 Perovskite Solar Cells *via* Numerical Optimization of Carrier Transport Materials (HTLs/ETLs), *Nanomaterials*, 2023, **13**(15), 2221.

2 E. Akman, T. Ozturk, W. Xiang, F. Sadegh, D. Prochowicz, M. M. Tavakoli, *et al.*, The effect of B-site doping in all-inorganic CsPbIxBr3−x absorbers on the performance and stability of perovskite photovoltaics, *Energy Environ. Sci.*, 2023, **16**(2), 372–403.

3 Z. Cheng, T. Liu, B. Zhao, F. Shen, H. Jin and X. Han, Recent advances in organic-inorganic composite solid electrolytes for all-solid-state lithium batteries, *Energy Storage Mater.*, 2021, **34**, 388–416.

4 M. R. A. Bhatti, A. Kernin, M. Tausif, H. Zhang, D. Papageorgiou, E. Bilotti, *et al.*, Light-Driven Actuation in Synthetic Polymers: A Review from Fundamental Concepts to Applications, *Adv. Opt. Mater.*, 2022, **10**(10), 2102186.

5 J. Chen, W. Zhou, Y. Quan, B. Liu, M. Yang, M. Chen, *et al.*, Ionic liquid additive enabling anti-freezing aqueous electrolyte and dendrite-free Zn metal electrode with organic/inorganic hybrid solid electrolyte interphase layer, *Energy Storage Mater.*, 2022, **53**, 629–637.

6 C. Wang, J. T. Kim, C. Wang and X. Sun, Progress and Prospects of Inorganic Solid-State Electrolyte-Based All-Solid-State Pouch Cells, *Adv. Mater.*, 2023, **35**(19), 2209074.

7 M. Forsyth, P. Meakin, D. R. MacFarlane and A. J. Hill, Free volume and conductivity of plasticized polyether-urethane solid polymer electrolytes, *J. Phys.: Condens. Matter*, 1995, **7**(39), 7601–7617.

8 X. Zhao, Y. Du, W. Li, Z. Zhao and M. Lei, Organic/inorganic hybrids for intelligent sensing and wearable clean energy applications, *Adv. Compos. Hybrid Mater.*, 2023, **6**(5), 176.

9 K. Zhou, Y. Zhou, Z. Jia, G. Ding, X. Q. Ma, W. Niu, *et al.*, Single-crystal metal-organic frameworks for electronic and opto-electronic devices, *Cell Rep. Phys. Sci.*, 2023, **4**(11), 101656.

10 X. Zhao, Y. Du, W. Li, Z. Zhao and M. Lei, Organic/inorganic hybrids for intelligent sensing and wearable clean energy applications, *Adv. Compos. Hybrid Mater.*, 2023, **6**(5), 176.

11 P. González-Izquierdo, O. Fabelo, L. Canadillas-Delgado, G. Beobide, O. Vallcorba, M. Sánchez-Andújar, *et al.*, Temperature evolution of (quinuclidinium)[FeCl4]: a plastic/polar magnetic hybrid compound with a giant dielectric constant, *J. Mater. Chem. C*, 2020, **8**(33), 11389–11398.

12 L. A. K. Staveley, Phase Transitions in Plastic Crystals, *Annu. Rev. Phys. Chem.*, 1962, **13**(1), 351–368.

13 A. Sohani, M. H. Shahverdian, S. Hoseinzadeh and M. El Haj Assad. Thermal energy storage systems. *Emerging Trends in Energy Storage Systems and Industrial Applications*. 2023, pp. 189–222.

14 J. Salgado-Beceiro, J. M. Bermúdez-García, A. L. Llamas-Saiz, S. Castro-García, M. A. Señarís-Rodríguez, F. Rivadulla, *et al.*, Multifunctional properties and multi-energy storage in the $[(CH_3)_3S][FeCl_4]$ plastic crystal, *J. Mater. Chem. C*, 2020, **8**(39), 13686–13694.

15 D. Li, X. M. Zhao, H. X. Zhao, L. S. Long and L. S. Zheng, Coexistence of Magnetic-Optic-Electric Triple Switching and Thermal Energy Storage in a Multifunctional Plastic Crystal of Trimethylchloromethyl Ammonium Tetrachloroferrate(III), *Inorg. Chem.*, 2018, **58**(1), 655–662.

16 J. Zhao, J. Sun, Y. Li, R. Xia, W. Zhang, B. Wang, *et al.*, Wood-plastic materials with organic–inorganic hybrid phase change thermal storage as novel green energy storage

composites for building energy conservation, *J. Mater. Sci.*, 2022, **57**(5), 3629–3644.

17 K. Ben Brahim, M. Ben gzaiel, A. Oueslati, K. Khirouni, M. Gargouri, G. Corbel, *et al.*, Organic–inorganic interactions revealed by Raman spectroscopy during reversible phase transitions in semiconducting [(C2H5)4N] FeCl4, *RSC Adv.*, 2021, **11**(30), 18651–18660.

18 D. Wyrzykowski, T. Maniecki, A. Pattek-Janczyk, J. Stanek and Z. Warnke, Thermal analysis and spectroscopic characteristics of tetrabutylammonium tetrachloroferrate(III), *Thermochim. Acta*, 2005, **435**(1), 92–98.

19 M. T. Hay and S. J. Geib, Tetrabutylammonium tetrachloroferrate(III), *Acta Crystallogr., Sect. E:Struct. Rep. Online*, 2004, **61**(1), m190–m191.

20 A. Le Bail, H. Duroy and J. L. Fourquet, Ab-initio structure determination of LiSbWO6 by X-ray powder diffraction, *Mater. Res. Bull.*, 1988, **23**(3), 447–452.

21 J. Rodríguez-Carvajal, Recent advances in magnetic structure determination by neutron powder diffraction, *Phys. B*, 1993, **192**(1–2), 55–69.

22 H. Chen, Z. Xia, J. Qi, H. Peng, Y. Bai, X. Shen, *et al.*, A Bendable Photoluminescent Molecular Crystal with Phase Transition Accompanied by SHG Switching, *Chin. J. Chem.*, 2025, **43**(22), 2922–2928.

23 Z. T. Xia, H. P. Chen, J. C. Qi, H. Peng, X. Shen, Y. J. Bai, *et al.*, A high phase transition temperature organic–inorganic Sn (IV)-based metal halide designed by applying amino positional isomerism to the cation, *Inorg. Chem. Front.*, 2025, **12**(7), 2825–2832.

24 M. Li, G. Xu, W. Xin and Y. Zhang, Switchable Dielectric Behavior and Order-Disorder Phase Transition in a New Organic-Inorganic Hybrid Compound: (CH3NH3)4[InCl6] Cl, *Eur. J. Inorg. Chem.*, 2020, **2020**(7), 626–630.

25 J. Salgado-Beceiro, S. Castro-García, M. Sánchez-Andújar and F. Rivadulla, Motional Narrowing of Electron Spin Resonance Absorption in the Plastic-Crystal Phase of [(CH3)4N]FeCl4, *J. Phys. Chem. C*, 2018, **122**(48), 27769–27774.

26 J. Walker, K. P. Marshall, J. Salgado-Beceiro, B. A. D. Williamson, N. S. Løndal, S. Castro-Garcia, *et al.*, Mesophase Transitions in [(C2H5)4N][FeBrCl3] and [(CH3) 4N][FeBrCl3] Ferroic Plastic Crystals, *Chem. Mater.*, 2022, **34**(6), 2585–2598.

27 H. Wang, A. Braun, S. P. Cramer, L. B. Gee and Y. Yoda, Nuclear Resonance Vibrational Spectroscopy: A Modern Tool to Pinpoint Site-Specific Cooperative Processes, *Crystals*, 2021, **11**(8), 909.

28 T. J. Kistenmacher and G. D. Stucky, Structural and spectroscopic studies of tetrachlorophosphonium tetrachloroferrate(III), [PCl4][FeCl4], *Inorg. Chem.*, 1968, **7**(10), 2150–2155.

29 A. Sabatini and L. Sacconi, Far-Infrared Spectra of Some Tetrahalo Metal Complexes, *J. Am. Chem. Soc.*, 1964, **86**(1), 17–20.

30 D. Lin-Vien, N. B. Colthup, W. G. Fateley and J. G. Grasselli, Preface. The Handbook of Infrared and Raman Characteristic Frequencies of Organic, *Molecules*, 1991, xv–xvi.

31 K. Nakamoto, *Infrared and Raman spectra of inorganic and coordination compounds, part B: applications in coordination, organometallic, and bioinorganic chemistry*, John Wiley & Sons, Inc., 2008, pp. 1–403.

32 D. Abid, I. Dhouib, P. Guionneau, S. Pechev, I. Chaabane, N. Daro, *et al.*, Proton conduction study of a new selenate-based hybrid compound, *J. Alloys Compd.*, 2020, **824**, 153826.

33 K. M. Batoo, N. A. Alimuddin and S. Kumar, Synthesisation, electrical and magnetic properties of Al doped nano ferrite particles, *Int. J. Nanopart.*, 2009, **2**(1/2/3/4/5/6), 416.

34 K. M. Batoo, S. Kumar and C. G. Lee, Influence of Al doping on electrical properties of Ni–Cd nano ferrites, *Curr. Appl. Phys*, 2009, **9**(4), 826.

35 A. M. M. Farea, S. Kumar, K. M. Batoo, A. Yousef and C. G. Lee, Structure and electrical properties of Co0.5CdxFe2.5−xO4 ferrites, *J. Alloys Compd.*, 2008, **464**(1–2), 361–369.

36 A. Ghoudi, S. Auguste, J. Lhoste, W. Rekik, H. Ghalla, K. Khirouni, *et al.*, Crystal Structure and Spectroscopic Characterization of a New Hybrid Compound, (C12H17N2) 2[CdBr4], for Energy Storage Applications, *ACS Omega*, 2024, **9**(26), 28339–28353.

37 A. Moulahi, O. Guesmi, M. S. M. Abdelbaky, S. García-Granda and M. Dammak, Structural characterization, thermal analysis, electric and dielectric properties of a novel organic-inorganic hybrid compound based on iron fluoride, *J. Alloys Compd.*, 2022, **898**, 162956.

38 S. Y. Ibrahim, E. Sheha and S. Abouelhassan, The effect of isothermal annealing on the AC conductivity of Polyvinyl Alcohol-based polymer as an energy storage system, *J. Basic Environ. Sci.*, 2024, **11**(4), 670–679.

39 G. E. Pike, ac Conductivity of Scandium Oxide and a New Hopping Model for Conductivity, *Phys. Rev. B*, 1972, **6**(4), 1572–1580.

40 S. R. Elliott, Temperature dependence of a.c. conductivity of chalcogenide glasses, *Philos. Mag. B*, 1978, **37**(5), 553–560.

41 A. C. Dhieb, A. Valkonen, M. Rzaigui and W. Smirani, Synthesis, crystal structure, physico-chemical characterization and dielectric properties of a new hybrid material, 1-Ethylpiperazine-1,4-diium tetrachlorocadmate, *J. Mol. Struct.*, 2015, **1102**, 50–56.

42 A. Ghoudi, K. Ben Brahim, H. Ghalla, J. Lhoste, S. Auguste, K. Khirouni, *et al.*, Crystal structure and optical characterization of a new hybrid compound, C6H9N2FeCl4, with large dielectric constants for field-effect transistors, *RSC Adv.*, 2023, **13**(19), 12844–12862.